Mapping of horizontal refrigerant two-phase flow patterns based on clustering of capacitive sensor signals

H. Canière, B. Bauwens, C. T'Joen and M. De Paepe

In: International Journal of Heat and Mass Transfer, Volume 53 (23-24), p.5298-5307, 2010.

H. Canière, B. Bauwens, C. T'Joen and M. De Paepe (2010). Mapping of horizontal refrigerant two-phase flow patterns based on clustering of capacitive sensor signals. *International Journal of Heat and Mass Transfer* 53(23-24) 5298-5307.
doi:10.1016/j.ijheatmasstransfer.2010.07.027

Mapping of horizontal refrigerant two-phase flow patterns based on clustering of capacitive sensor signals

H. Canière[1], B. Bauwens[2], C. T'Joen[1,3] and M. De Paepe[1]

[1]Department of Flow, Heat and Combustion Mechanics, Ghent University-UGent
St.-Pietersnieuwstraat 41, 9000 Gent, Belgium
[2]Department of Electrical Engineering, Systems and Automation, Ghent University-UGent,
Gebouw Regeltechniek, Technologiepark 913, 9052, Zwijnaarde, Belgium
[3]Department Radiation, Radionuclides & Reactors, Delft University of Technology
Mekelweg 15, 2629 JB Delft, The Netherlands

Corresponding author
Hugo Canière
Hugo.Caniere@UGent.be
Tel: +32 9 264 32 89
Fax: +32 9 264 35 75

Abstract
A capacitive void fraction sensor was developed to study the objectivity in flow pattern mapping of horizontal refrigerant two-phase flow in macroscale tubes. Sensor signals were gathered with R410A and R134a in a smooth tube with an inner diameter of 8mm at a saturation temperature of 15°C in the mass velocity range of 200 to 500 kg/m²s and vapour quality range from 0 to 1 in steps of 0.025. A visual classification based on high speed camera images is made for comparison reasons. A statistical analysis of the sensor signals shows that the average, the variance and a high frequency contribution parameter are suitable for flow regime classification into slug flow, intermittent flow and annular flow by using the fuzzy c-means clustering algorithm. This soft clustering algorithm predicts the slug/intermittent flow transition very well compared to our visual observations. The intermittent/annular flow transition is found at slightly higher vapour qualities for R410A compared to the prediction of [Barbieri et al., 2008, Flow patterns in convective boiling of refrigerant R134a in smooth tubes of several diameters, 5th European Thermal-Sciences Conference, The Netherlands]. An excellent agreement was obtained with R134a. This intermittent/annular flow transition is very gradual. A probability approach can therefore better describe such a transition. The membership grades of the cluster algorithm can be interpreted as flow regime probabilities. Probabilistic flow pattern maps are presented for R410A and R134a in an 8 mm I.D. tube.

Keywords: two-phase flow regimes, HFC, flow pattern map, fuzzy c-means clustering

Nomenclature

AVG	average
CPSD	cumulative power spectral distribution
c	centroid
C	regression coefficient
D	inner tube diameter, m
Fr	Froude number
G	mass velocity, kg/m^{2}s
c_p	specific heat capacity, J/kgK
h	specific enthalpy, J/kg
J	objective function
K	number of features
m	mass flow rate, kg/s
n	regression coefficient
N	number of objects/data points
NC	number of clusters
M2	variance
M3	skewness
M4	kurtosis
MG	membership grade
P	flow regime probability
PDE	probability density estimation
PSD	power spectral density
T	temperature, K
u	cluster fraction
V	voltage signal, V
var	variance
w	weight parameter
x	vapour quality, -
X_{tt}	Lockhart-Martinelli parameter

Greek symbols

Δ	difference
σ	variance
μ	mean

Subscripts

A	annular flow
i, i'	class index
I	intermittent flow
j	object index
k	feature index
L	liquid
max	maximum
min	minimum
PH	preheater
R	refrigerant
S	slug flow
sat	saturation
V	vapour
2PH	two-phase

Superscripts

*	dimensionless
m	smoothness factor

1. Introduction

Complex two-phase flow phenomena occur during the phase change of refrigerant from liquid to vapour and vice versa. To accurately predict the heat transfer and pressure drop, these flow phenomena should be incorporated in the design models for in-tube evaporators used in refrigeration and air-conditioning [1-2]. Traditionally, this is achieved by classifying two-phase flows into flow regimes and presenting them in flow pattern maps. Kattan et al. [3-4] introduced a comprehensive flow pattern map in the heat transfer prediction of boiling refrigerants. Recently, Cheng et al. [5] published a comprehensive review on flow regimes and flow pattern maps. Most of the two-phase flow classifications are based on visualizations (with or without use of high speed cameras). But visual-only methods are inherently subjective. Cheng et al. [5] assign this as the main reason why flow pattern data from different researchers are often inconsistent for similar test conditions. Objective methods can therefore contribute to more accurate flow pattern data.

Rather than purely classifying a flow into mutually exclusive regimes, the classification problem can also be approached by describing the flow as a combination of different flow regimes each with a certain probability. Nino et al. [6] introduced the probabilistic approach in multiport microchannels. Jassim and Newell [7] applied probabilistic flow regime mapping to predict pressure drop and void fraction in microchannels. Van Rooyen et al. [8] used the same approach for intermittent flows during condensation in macroscale tubes. Jassim et al. [9] obtained probabilistic two-phase flow data of R134a and R410A in single horizontal smooth, adiabatic tubes (diameters D ranging from 1.74mm to 8mm) by using an automated image recognition technique. Jassim [10] also developed curve fits for this time fraction data, which were used by Jassim et al. [11] for void fraction modeling and by Jassim et al. [12] for heat transfer modeling during condensation. However, so far, it is not known how general such time fraction curve fits are [5].

This study aims to find more objectivity in flow pattern mapping. Therefore a capacitance probe was developed [13][14] as well as a transducer suitable for use with low dielectric fluids such as refrigerants [15]. The use of a signal clustering technique was previously investigated for air-water flows [16] and is now further studied for use with evaporating refrigerant flows to objectively and probabilistically describe flow regime transitions.

2. Experimental facility

2.1 Refrigerant test facility

In Figure 1, a schematic of the refrigerant test facility is shown. A pump provides subcooled refrigerant to the preheater. This preheater consist of six tube-in-tube heat exchangers with a total length of 15m. The length of the preheater can be altered between 1m and 15m in steps of 1m. The refrigerant in the central tube is heated and evaporated to the desired vapour quality x, by hot water flowing in the annuli. A boiler system heats a 2m³ tank to provide hot water at a stable temperature during the experiments. The conditioned vapour-liquid mixture is fed into the test sections after which it is condensed back to liquid in a plate condenser. The condenser transfers the heat from the refrigerant to a water/glycol (30%) flow and provides subcooled liquid to the pump. The ice water is supplied from a 1m³ tank which is cooled by a chiller system. In contrast with a traditional compressor loop, there is only one working pressure. The pump only bridges the pressure losses. By controlling the frequency of the pump the mass velocity G, in the refrigerant loop is set. The loop is connected to a reservoir which is submerged in a water bath. By changing the bath temperature, the saturation pressure in the loop can be altered.

The mass flow rate of the refrigerant as well as the mass flow rate of the water in the preheater, are measured using coriolis type flow meters with an accuracy of ±0.2% (of reading). Temperature measurements are performed using thermocouples (type K) which are in situ calibrated with an uncertainty of ±0.05°C. From these measurements, the heat balance of the preheater is determined (Eq. (1)).

$$m_R\left(h_{R,PHout} - h_{R,PHin}\right) = m_{w,PH}c_{p,w}\left(T_{w,PHin} - T_{w,PHout}\right) \tag{1}$$

$$x_{PH} = \frac{h_{R,PHout} - h_{R,L}}{h_{R,V} - h_{R,L}} \tag{2}$$

The uncertainty in this heat balance is monitored online. Measurements were accepted if the uncertainty in the heat balance was smaller than ±2% (with an exceptional ±4% for

G=200kg/m²s and x<0.125) and all temperature measurements of the preheater were stable within the uncertainty of ±0.05°C over the course of the measurements. The uncertainty in the mass velocity is smaller than 1.5% at mass velocities lower than 250 kg/m^{2}s and smaller than 0.75% for mass velocities higher than 250 kg/m^{2}s. The vapour quality at the inlet of the test section is calculated using Eqs. (1)-(2). The uncertainty in x varied between ±0.005 and ±0.02 with the higher values for higher vapour qualities. The saturation temperature at the exit of the preheater was controlled to within ±0.5°C.

2.2 Adiabatic test section

A horizontal adiabatic test section is used for flow visualization and characterization purposes. It consists of a sight glass with a camera, the capacitive void fraction sensor and a second sight glass. The second sight glass after the capacitance sensor is required to ensure electrical separation between the set-up and the sensor. This is absolutely necessary to prevent noise pick-up in the capacitance sensor by the antenna effect of the copper tubing. To eliminate disturbances from bends or valves, a minimum entrance and exit length of 60D was ensured upstream and downstream of the test section. In that case, the flow in the test section is fully developed and a constant tube diameter is assured over the full length of the test section with as little disturbances as possible.

The sight glasses are made of smooth quartz glass (100mm x 8mm inner diameter/10mm outer diameter) which is mounted in the 7.91mm copper tube. Nylon ferrules are used as sealing in the fittings. The glass tube was annealed and hardened to prevent fracture caused by micro cracks at higher pressure. Two bolt connections are used in parallel with the sight glasses to absorb the axial forces. To ensure the electrical separation of the tubing, the supports for these bolts are made of electrically insulating material. The construction was successfully pressure and leak tested with nitrogen up to 40bar. To capture images of the refrigerant flow, a monochromatic high speed camera was used which could capture images at 250 frames per second.

2.3 Capacitive void fraction sensor

A capacitance probe with a concave electrode configuration was developed for dynamic two-phase flow void fraction measurements [13][17]. Capacitance probes use the difference in dielectric constant between the liquid phase and the vapour phase. The output of the probe is a voltage signal proportional to the capacitance of the two-phase mixture between the electrodes. To acquire (quasi)-local two-phase flow data, the electrode width is equal to the diameter of the tube. In Figure 2 the electrode configuration is illustrated. The capacitance between the middle electrode pair is measured. The outer electrode pairs are used for guarding purposes.

The electronic transducer measures the capacitance between the electrodes at 2MHz and is based on the charge-discharge principle [15][17]. The electric current that flows because of this charging and discharging is converted to a voltage signal. These voltage signals are gathered at a sample frequency of 1kHz by the DAQ system and are made dimensionless according to Eq. (3). V_L and V_V are the voltage levels of liquid only and vapour only flowing in the tube.

$$V^* = \frac{V_{2PH} - V_V}{V_L - V_V} \tag{3}$$

The transducer gain is 1.16V/pF. At 15°C, the difference between V_L and V_V was measured ΔV=1.32V for R410A and ΔV=1.31V for R134a. The difference in electric capacitance between liquid flow and vapour flow is thus 1.14pF and 1.13pF respectively. A temperature variation of ±0.5°C results in variations of V_L of ±6mV or ±0.44% of ΔV. The slope of the V_L-T curve is -0.0117 V/°C for R410A and -0.0099 V/°C for R134a. The negative slope of the V_L-T calibration curve corresponds to the decreasing dielectric constant of liquid refrigerant in function of temperature. The influence of temperature on the dielectric constant of the vapour phase is negligible. A temperature compensation was thus only performed to V_L. After this compensation, all measurements of V_L and V_V fell within ±4mV. There was no significant difference in V_L or V_V between measurements at the start and those taken at the end of the experimental campaign. Drift from the electronic transducer can therefore be neglected. The noise level of both liquid only and vapour only flow is 10mV (peak to peak). The corresponding uncertainty evaluated as 2σ is ±4mV or ±0.3% of ΔV, resulting in signal-to-noise ratios SNR higher than 300. The step response of the transducer to a change in capacitance of 1pF was faster than the sample frequency (1kHz).

3. Experimental results

3.1 Dataset and visual classification

Capacitance sensor signals are gathered for R410A at T_{sat}=15°C. Four data series at mass velocities ranging from G=200 to 500 kg/m^{2}s are obtained with vapour qualities ranging from 0 to 1 in steps of 0.025. A similar set was gathered with R134a. But the G=400 kg/m²s and G=500 kg/m²s series are not complete up to x=1. Because of the larger pressure drop of R134a, the saturation temperature could not be kept constant at 15°C. In Figure 3, the dataset with our visual classification is shown in a Wojtan-Ursenbacher-Thome flowmap [19] under adiabatic conditions. Additionally the intermittent/annular flow transition of Barbieri et al. [20] is depicted as well (Eq. (4)).

$$G_{I-A}^2 = 3.75 g D \frac{(1-x)^{0.16}}{x^{2.16}} \frac{\rho_V^{1.2}}{\rho_L^{-0.8}} \left(\frac{\mu_L}{\mu_V}\right)^{0.24} \tag{4}$$

Using the high speed camera images, the observed two-phase flows were classified into slug flow, intermittent flow and annular flow. The liquid slugs have to fill the entire tube but can be aerated to be classified as slug flow. In annular flow, the motion of the liquid flowing at the top of the tube should be comparable to the motion of liquid flowing at the bottom. Intermittent flow groups the remaining two-phase flows.

The slug flow/intermittent flow transitions have the same trend but do not fully agree with our visual classification. This discrepancy can be partially due to the classification criterion. Wojtan et al. [19] define the intermittent flow regime as a group of unsteady flow patterns like plug and slug flows. Due to the unsteadiness of the flow, the entire tube periphery is frequently wetted in this flow regime, but does not have to remain wet all the time. In our classification, the presence of the slugs itself is the criterion. For R410A, at G>300kg/m²s, slugs do appear but the flow is classified as intermittent by Wojtan et al. [19]. At G=200kg/m^{2}s and x>0.15, no slugs appear in our observations, although slugs should be present according to their flow pattern map. For R134a, at G=200kg/m²s and x>0.125 again no slugs were observed even though predicted by the flow pattern map. At higher mass velocities, the transition line corresponds well to our visual classification. There is a possibility that high amplitude waves are classified as highly aerated slugs. This can shift the transition line to higher vapour qualities.

In the flow pattern map of Wojtan et al. [19] the intermittent-annular flow transition is defined at a constant value of the Lockhart-Martinelli parameter X_{tt}=0.34. Thus, only density and viscosity are taken into account, resulting in a transition line at constant vapour quality. However, Barbieri et al. [20] concluded from their visual observations that this transition is also affected by tube diameter, mass velocity and vapour quality. They proposed a transition line as a function of the liquid Froude number and X_{tt} based on observations of R134a two-phase flows in smooth tubes with internal diameters varying from 6.2mm to 12.6 mm at T_{sat}=5°C, namely $Fr_L = 3.75\ X_{tt}^{2.4}$. Thus also mass velocity and tube diameter are accounted for. Their transition line in G-x format (Eq. (4)) is set out in dash-dot in Figure 3 and agrees much better with our visual observations compared to the transition of Wojtan et al. [19]. In Figure 4 the data of Barbieri et al. and their regression is shown together with our new data of R134a and R410A in an 8mm tube at T_{sat}=15°C. The slope of our R134a data corresponds well to the regression of Barbieri et al. [20]. The slope of our R410A data is slightly steeper. But, the Fr_L-X_{tt} map shows that our new data is located within the scatter cloud of the Barbieri et al. data. Therefore, the Barbieri et al. [20] criterion for intermittent-annular flow transition is found to be valid for the conditions at T_{sat}=15°C and for use with R410A.

No dry-out was observed at high vapour qualities, although this is predicted by the flow pattern map of Wojtan-Ursenbacher-Thome. But the observations were done under adiabatic conditions and fully developed flow. There is no reason why there should be partial dry-out or a transition to stratified-wavy flow. Under diabatic conditions, dry-out appears because the liquid film is thinner at the top of the tube. This allows dry patches to appear before new liquid is provided from the thicker film at the bottom. Under fully developed adiabatic conditions, the liquid can swing back to the top of the tube. The velocity in the vapour core is definitely high enough to preserve the annular film because this velocity increases with vapour quality. So, the liquid film thins out when the vapour quality is increased until all liquid is vaporized or entrained.

3.2 Capacitive void fraction signals

Three typical sensor signals are shown in Figure 5, i.e. a slug flow, an intermittent flow and an annular flow signal obtained with R410A at T_{sat}=15°C. At low vapour qualities slugs frequently fill the entire cross section with liquid. The slugs are often aerated with vapour bubbles. The concentration of these bubbles is higher near the top of the tube. Each liquid slug causes a peak in the voltage signal that approaches $V^*=1$. This results in a high variance in the signal values. The slug frequencies dominate the frequency spectrum. The average signal values of slug flows are high due to the large liquid content.

At transition from slug flow to intermittent flow, the vapour content in the slugs is that high, that the liquid bridges break up. The interfacial waves are more turbulent in the intermittent flow regime, causing liquid droplets to swing into the vapour phase and vapour bubbles to appear into the liquid phase. The two-phase flow becomes fully chaotic. This results in a higher frequency spectrum content at frequencies higher than 5Hz. The tube perimeter remains fully wetted. The amplitude of the wave patterns diminishes and the liquid content in the upper film increases gradually.

A further increase in vapour quality results in the development of an annular film. The thickness of the film always remains larger at the bottom of the tube. The transition from intermittent to annular flow is very gradual. In fully developed annular flow, the interface between the liquid annulus and the vapour core is disturbed by small amplitude waves. Droplets may be dispersed in the vapour core but these are hard to notice due to the limited visual access. The annular film thickness gradually diminishes with increasing x. The average signal values are low because of the high vapour content, the variance of the signal values is low as well, but the frequency content at high frequencies is high instead.

4. Statistical analysis

4.1 Feature definitions

From each signal of the dataset, several statistical features are mined. A first group consists of the statistical moments of the sensor signal, i.e. the average value (AVG), the variance (M2), the skewness (M3) and the kurtosis (M4). These features determine the shape of the probability density estimation (PDE) of a signal and represent information of the signal in the amplitude domain. A second group consists of features in the frequency domain, further caller F#-parameters. First, the power spectral density (PSD) was calculated using the fast Fourier algorithm. Then the cumulative distribution (CPSD) was taken of the PSD contributions between 0 and 100Hz. The features are then the frequencies corresponding to a certain percentile of this cumulative distribution. For example F50 is the frequency corresponding to the 50% percentile of the CPSD. This means that 50% of the power spectrum contribution (between 0-100Hz) is present in the frequencies lower than F50. The frequency range for vapour-liquid interface phenomena is typically smaller than 100Hz [21]. Therefore, only contributions of frequencies lower than 100Hz are considered.

When following a trajectory (in a flow pattern map) from intermittent flow to annular flow, typically the power spectrum contributions of low frequencies (related to pseudo-slugs for instance) diminish and the power spectrum contributions of higher frequencies (related to interfacial phenomena of annular film flow) increase. The purpose of the F#-parameters is to incorporate this effect of PSD contributions moving to higher frequencies and so track the intermittent-annular flow transition. However, in the annular flow regime at very high vapour qualities, some very low frequent phenomena were noticed, most probably induced by dry-out phenomena in the preheaters. This causes drastic drops in the F#-parameter values. Since this is not related to the intermittent to annular flow transition, this phenomenon should not contribute to the F#-parameters. Therefore, a regression was performed to the F#-parameter data eliminating the data at high vapour quality with low F#-parameter values. This regression, using sigmoid functions (Eq. (5)) also eliminates the inherent scatter in the frequency parameter data. This all is shown in Figure 6.

$$y = \frac{c}{1 + \exp[-a(x-b)]} \tag{5}$$

4.2 Fisher criterion

The signal features are investigated for their ability of flow regime classification. First, a *Fisher Criterion* [22] was applied to the datasets of R410A and R134a using the visual classification into slug flow, intermittent flow and annular flow. A Fisher discriminant

$J_{ii'}(k)$ is determined using Eq. (6), with $\mu_i(k)$ the mean of feature k of the data points in class i and $\sigma_i(k)$ the variance of feature k of the data points in class i.

$$J_{ii'}(k) = \frac{\left[\mu_i(k) - \mu_{i'}(k)\right]^2}{\sigma_i(k) + \sigma_{i'}(k)} \tag{6}$$

The score of the Fisher Criterion for a selected feature is then the average of $J_{ii'}$ for all combination of classes i and i'. This criterion quantitatively determines whether a feature is able to separate class i from class i'. It expresses how far the means of the classes are separated taking also the variances within the classes into account.

The results are listed in Table 1 and Table 2 for R410A and R134a respectively. If the Fisher criterion is applied to the full datasets, AVG and M2 have a significantly larger score compared to M3 and M4. If the intermittent flow data and the annular flow data are grouped in a non-slug flow class, then the score of the variance is dominant (S/non-S in Tables 1 and 2). Due to the presence of liquid slugs a second maximum in the PDE at high vapour qualities appears, causing M2 to be significantly larger compared to M2 of non-slug flows. The variance thus has the highest potential in separating slug flows from non-slug flows. This transition occurs in a narrow zone in the flow pattern map. The same conclusion applies if the Fisher criterion is evaluated using only slug flow and intermittent flow data (see S-I only in Tables 1 and 2). When slug flow data and intermittent flow data are grouped into a non-annular flow class, AVG has the highest score of the features in the amplitude domain. This feature is thus useful for tracking the intermittent/annular flow transition. In contrast with M2, AVG decreases smoothly with increasing vapour quality. It is basically a measure for average void fraction. No sudden change in the trend appears in the transition zone from intermittent flow to annular flow.

Concerning the F#-parameters, the F95 has the highest score for all data of R134a and the second highest score for the R410A data. Since these parameters were defined for tracking the change in frequency contributions in the intermittent /annular flow transition, they have the highest scores for the annular/non-annular division and the intermittent-annular only data. According to the Fisher criterion, F95 has the highest potential in separating intermittent from annular flow signals.

4.3 Principle Component Analysis

Another possible approach for reducing the number of features is performing a *Principle Component Analysis* (PCA) [23]. In a PCA the eigenvalues and eigenvectors of the covariance matrix of the feature data are calculated. The first eigenvector in feature space (with the highest eigenvalue) indicates the major direction in the feature data cloud. The coefficients of this first eigenvector thus indicate the (relative) importance of the features. Applying a PCA to the HFC datasets, the eigenvalue of the first principle component is about ten times higher than that of the second principle component. The data cloud is thus mainly organized along one direction. The coefficients of the first principle component in the feature space are listed in Table 3. The PCA again proves the dominance of AVG and M2 over M3 and M4.

The F#-parameters equally contribute to the first principle component. This means that any of these parameters can be chosen, but according to the Fisher test, F95 is the best choice for the classification. Comparing the relative importance of the amplitude domain features and the frequency domain features, the F#-parameters are slightly higher but the coefficients of both groups are in the same order of magnitude.

The feature space of AVG, M2 and F95 is shown in Figure 7. From this plot, it is again clear that finding the slug/intermittent flow transition will be feasible by using M2. But the intermittent/annular flow transition is rather arbitrary due to the smoothness of this transition.

The multivariate analysis of the sensor signal features thus results in a small selection of features which contain the necessary flow regime information. The Fisher Criterion indicates the AVG, M2 and F95 as optimal for flow pattern classification. A principle component analysis supports this. The choice of the features can be related to the two-phase flows as follows: AVG is a matter for void fraction, M2 is directly related to the presence of liquid slugs and F95 parameter can track the power spectrum contribution shift towards higher frequencies in the intermittent-annular flow transition.

5. Fuzzy c-means clustering

Clustering algorithms [24] are unsupervised learning methods. The goal of such a method is to deduce properties from a dataset, without the help of a supervisor providing correct answers for each observation. In the case of two-phase flow classification, no visual decisions are needed. Clustering analysis tries to group a collection of objects into subsets or clusters such that those within each cluster are more closely related to one another than objects assigned to different clusters. An object is a selection of input features deduced from a sensor signal. The choice of these input features is fundamental to the clustering technique. The choice of a dissimilarity measure between two objects, the distance function, is a second important factor. By far the most common choice of the distance function is the squared or Euclidian distance between two objects y_j and $y_{j'}$ (Eq. (7)).

$$d(y_j, y_{j'}) = \sum_{k=1}^{K} w_k (y_{kj} - y_{kj'})^2 \tag{7}$$

This is a weighted average of squared feature distances with w_k the weight parameters and y the positions of the objects in feature space. Each object is iteratively assigned to one cluster based on the minimization of an objective function. Each of the weight parameters can be chosen to set the relative importance of the features upon the degree of similarity of the objects. Variables that are more relevant in separating the clusters should of course be assigned a higher influence in defining object dissimilarity.

The fuzzy c-means clustering algorithm is a soft-clustering algorithm. This means that each data point is assigned to a cluster to some degree that is specified by a membership grade *MG*. This allows for describing the boundaries between clusters in a smooth way. Since the aim of the clustering of our datasets is finding a probabilistic description of flow regime boundaries, this soft-clustering algorithm is the preferred choice amongst other clustering algorithms like k-means clustering or hierarchical clustering.

The user first has to choose the number of clusters *NC*. The fuzzy c-means clustering algorithm then starts with initial guesses for the centers (or centroids) of each cluster c_i. Initial cluster fractions u_{ij} are also assigned to each data point in such a way that:

$$\sum_{i=1}^{NC} u_{ij} = 1 \tag{8}$$

The algorithm minimizes an objective function J_m (Eq. (9)) based on the distance between a data point x_j and a cluster centroid c_i.

$$J_m = \sum_{j=1}^{N}\sum_{i=1}^{NC} u_{ij}^m \left\| x_j - c_i \right\|^2 \qquad 1 \le m \le \infty \tag{9}$$

The parameter m (chosen at the default value 2) determines the smoothness of the cluster transitions. When m approaches 1, the cluster boundaries are sharp, when m approaches infinity, u_{ij} becomes constant over all data. The values of u_{ij} and c_i are iterated from an initial value until convergence using Eqs. (10)-(11). The default value (1e-5) for the minimum amount of improvement of the objective function is used as convergence criterion.

$$u_{ij} = \sum_{k=1}^{K} \left(\frac{\left\| x_j - c_i \right\|}{\left\| x_j - c_k \right\|} \right)^{-\frac{2}{m-1}} \tag{10}$$

$$c_i = \frac{\sum_{j=1}^{N} u_{ij}^m x_j}{\sum_{j=1}^{N} u_{ij}^m} \tag{11}$$

The output of the clustering algorithm is thus a membership grade *MG* of each class for every data point. A membership grade of unity means the sensor signal is typical for that class. The data point is assigned to the class for which it has the highest membership grade.

The fuzzy c-means clustering algorithm is applied to the refrigerant flow signal data using a combination of input features which can track both the slug flow/intermittent flow and the intermittent flow/annular flow transition: i.e. the feature input matrix $I = w\cdot[AVG, M2, F95]$. $w_k=1/(2var_k)$ represents the weight parameters listed in Table 4. By using these values every feature equally contributes to the clustering [24]. This selection of features is based on the multivariate analysis and has a clear physical link with the flow phenomena. The result of using these features to cluster the dataset into three clusters is shown in Figure 8. The clustering groups the data points in perfectly separable areas in the flow map. Compared to our visual classification (Figure 3) an excellent agreement is found. The slug/intermittent flow transition is perfectly predicted as is the intermittent/annular flow transition for R134a. The intermittent/annular flow transition for R410A however is found at slightly higher vapour qualities. The difference in vapour quality at the transition is less than 0.1 and can be assigned to the gradual nature of the transition and the subjectivity in visually classifying the flow regimes.

The corresponding membership grades are depicted in Figure 9. Because of the properties of the algorithm, they decline for vapour qualities smaller than the typical slug flow data point and vapour qualities larger than the typical annular flow data point. Therefore some post-processing was necessary to use the membership grades as flow regime probabilities.

First, the maxima and minima of the slug flow and annular flow membership grades are traced for each mass velocity series. These *MG* are kept constant at the maximum and minimum value outside the vapour qualities corresponding to the maxima and minima. The *MGs* of intermittent flow are then recalculated using Eq. (12). This recalculation does not affect the transitions, but only the data points near x=0 and x=1.

$$MG_I = 1 - MG_S - MG_A \tag{12}$$

The membership grades are now consistent with the probabilistic flow regime approach and can be interpreted as flow regime probabilities P. To generalize the probabilities, a regression is performed for every mass velocity series. Chapman functions (Eq. (13)) are used for the slug flow probabilities and sigmoid functions (Eq. (14)) for the annular flow probabilities.

$$P_S^* = P_0 + a\left[1 - \exp(-bx)\right]^c \tag{13}$$

$$P_A^* = \frac{1}{1 + \exp\left[-a(x-b)\right]} \tag{14}$$

Because of the residuals of the regression, a final rescaling is necessary using Eq. (15) to make the maximum probability unity and the minimum zero. This rescaling has only a significant effect for G=200kg/m²s and G=300kg/m²s. Finally the probability for intermittent flow is found (Eq. (16)). In Table 5 and Table 6, the regression coefficients with corresponding R-squared values are shown, as well as the necessary scaling factors.

$$P = \frac{P^* - p_{\min}}{p_{\max} - p_{\min}} \tag{15}$$

$$P_I = 1 - P_S - P_A \tag{16}$$

6. Probabilistic flow pattern mapping

6.1 Flow regime probabilities

In Figure 10, the probabilistic flow maps are presented for adiabatic flow of R410A and R134a at T_{sat}= 15°C in a horizontal smooth tube of 8mm I.D. at mass velocities ranging from 200 to 500 kg/m^{2}s and vapour qualities from 0 to 1. The flow regime probabilities P are shown as contour lines in the flow map. Our visual classification and the Wojtan-Ursenbacher-Thome flow map [19] with the extra intermittent/annular flow transition of Barbieri et al. [20] are depicted as well. The 50% probabilities are drawn in black. These correspond to the classification lines used by the clustering algorithm. It is very clear that the slug flow/intermittent flow transition is a narrow transition zone in the flow pattern map. This is now quantified in terms of the probabilities. The contour lines indicate a width of approximately Δx=0.05. The intermittent/annular flow transition instead is very gradual with a width of over Δx=0.25.

These flow regime probabilities are solely based on the capacitive void fraction signals. The void fraction variations of the two-phase flows are therefore explicitly used in these probabilistic flow pattern maps. The time fraction functions of Jassim et al. [9] instead are based on processing of images and thus track variations in the vapour-liquid interfaces. Since void fraction is the key parameter in the heat transfer models, these void fraction variations are more promising for improving heat transfer modeling.

6.2 Prediction method for the intermittent/annular flow transition

To generalize the flow regime probabilities found by the cluster method, a prediction method is developed for the flow transition between intermittent and annular flow. An adopted Barbieri et al. [20] equation (Eq. (17)) is proposed because its suitability was shown in §3.1. In this new prediction method, also the width of the transition zone is considered by incorporating the flow regime probabilities P in the regression coefficients C and n (Eqs. (18) and (19)). P_A is the annular flow regime probability which can be evaluated between 0 and 1.

$$Fr_L = CX_{tt}^n \tag{17}$$

$$C = 14.27P_A + 2.315 \tag{18}$$

$$n = -0.618P_A^2 + 0.6975P_A + 2.504 \tag{19}$$

The coefficients of determination, R^2, are 0.989 and 0.939 for C and n respectively. The R^2 values of the fit of the vapour quality for given flow regime probabilities and mass velocities are 0.973 for R134a and 0.974 for R410A. The mean absolute deviation of vapour quality is only 0.0164 for R134a and 0.0162 for R410A.

6.3 Applicability

This probabilistic flow regime transition between intermittent to annular flow can for instance be incorporated in the flow pattern based heat transfer model of Wojtan-Ursenbacher-Thome [25] to better describe the gradual change in flow characteristics in the intermittent to annular flow transition. The heat transfer prediction in this transition zone suffers from an inappropriate combination of flow structures at low mass velocities [17]. Using the flow regime probabilities will assure a proper weighing of the flow phenomena and result in a smooth transition. This can be an alternative for a full probabilistic heat transfer model for evaporating flow similar to the model developed by Jassim et al. [12] under condensing conditions.

7. Conclusions

A capacitance probe and transducer was developed for use with HFC refrigerants. Sensor signals are gathered with R410A and R134a in an 8mm I.D. smooth tube at a saturation temperature of 15°C in the mass velocity range of 200 to 500kg/m²s and vapour quality range from 0 to 1 in steps of 0.025. A visual classification based on high speed camera images is made for comparison reasons. This visual classification confirmed the new intermittent/annular flow transition criterion of Barbieri et al. [20] for use with R410A and T_{sat}=15°C.

The signal average, the variance and a frequency contribution parameter are found suitable for flow regime classification into slug flow, intermittent flow and annular flow. The use of the c-means fuzzy clustering algorithm is investigated for objective flow regime classification purposes. The clustering in feature space groups the data points in clearly separable areas in a flow pattern map. The slug flows could be easily separated from non-slug flows by using the variance of the sensor signal. The AVG and the F95 parameter were found most suitable for separating intermittent flows from annular flows. But, because of the gradual nature of this transition, the choice of this parameter is rather arbitrary.

The soft-clustering algorithm assigns a membership grade to each data point which can be interpreted as a flow regime probability. After regression of these membership grades, flow regimes probability functions were given and probabilistic flow pattern maps were presented for the HFC data. These maps clearly quantify the width of the transition zones. A probabilistic prediction method for the intermittent/annular flow transition is proposed based on the Barbieri et al. [20] correlation. This method can be further applied for probabilistic heat transfer and/or pressure drop modeling.

Acknowledgments

The authors would like to express gratitude to the BOF fund (B/06634) of the Ghent University - UGent which provided support for this study and thank Robert Gillis and Patrick De Pue for their technical experience and help. Also special thanks to ir. L. Colman (Vakgroep Electronica, Departement Toegepaste Ingenieurswetenschappen, Hogeschool Gent, Belgium) and ir. G. Colman (Intec_Design, Department of Information Technology, Ghent University, Belgium) for the development of the capacitance transducer.

References

1. J.R. Thome, Two-phase heat transfer using no-phase flow models?, Heat Transfer Engineering 25 (6) (2004) 1-2.
2. L. Liebenberg, J.P. Meyer, A review of flow pattern-based predictive correlations during refrigerant condensation in horizontally smooth and enhanced tubes, Heat Transfer Engineering 29 (1) (2008) 3-19.

3. N. Kattan, J.R. Thome, D. Favrat, Flow boiling in horizontal tubes: Part 1 - Development of a diabatic two-phase flow pattern map, Journal of Heat Transfer-Transactions of the ASME 120 (1) (1998) 140-147.
4. N. Kattan, J.R. Thome, D. Favrat, Flow boiling in horizontal tubes: Part 3 - Development of a new heat transfer model based on flow pattern, Journal of Heat Transfer-Transactions of the ASME, 120 (1) (1998) 156-165.
5. L.X. Cheng, G. Ribatski, J.R. Thome, Two-phase flow patterns and flow-pattern maps: Fundamentals and applications, Applied Mechanics Reviews 61 (5) (2008) 050802:1-28.
6. V.G. Nino, P.S. Hrnjak, T.A. Newell, Two-phase flow visualization of R134A in a multiport microchannel tube, Heat Transfer Engineering 24 (1) (2003) 41-52.
7. E.W. Jassim, T.A. Newell, Prediction of two-phase pressure drop and void fraction in microchannels using probabilistic flow regime mapping, International Journal of Heat and Mass Transfer 49 (15-16) (2006) 2446-2457.
8. E. van Rooyen, M. Christians, L. Liebenberg, J.P. Meyer, Optical measurement technique for predicting time-fractions in two-phase flow, Proceedings of the 5th International Conference on Heat Transfer, Fluid Mechanics and Thermodynamics (HEFAT), Sun City, South-Africa, 2007.
9. E.W. Jassim, T.A. Newell, J.C. Chato, Probabilistic determination of two-phase flow regimes in horizontal tubes utilizing an automated image recognition technique, Experiments in Fluids 42 (4) (2007) 563-573.
10. E.W. Jassim, Probabilistic flow regime map modeling of two-phase flow, PhD thesis, University of Illinois, Urbana-Champaign, IL, USA, 2006.
11. E.W. Jassim, T.A. Newell, J.C. Chato, Prediction of refrigerant void fraction in horizontal tubes using probabilistic flow regime maps, Experimental Thermal and Fluid Science 32 (5) (2008) 1141-1155.
12. E.W. Jassim, T.A. Newell, J.C. Chato, Prediction of two-phase condensation in horizontal tubes using probabilistic flow regime maps, International Journal of Heat and Mass Transfer 51 (3-4) (2008) 485-496.
13. H. Canière, C. T'Joen, A. Willockx, M. De Paepe, M. Christians, E. van Rooyen, L. Liebenberg, J.P. Meyer, Horizontal two-phase flow characterization for small diameter tubes with a capacitance sensor, Measurement Science & Technology 18 (9) (2007) 2898-2906.
14. H. Canière, C. T'Joen, A. Willockx, M. De Paepe, Capacitance signal analysis of horizontal two-phase flow in a small diameter tube, Experimental Thermal and Fluid Science 32 (3) (2008) 892-904.
15. G. Colman, H. Canière, L. Colman, M. De Paepe, Fast response capacitance transducer for online measurements of low dielectric fluid two-phase flow, IEEE Transactions on Instrumentation and Measurement (under review)

16. H. Canière, B. Bauwens, C. T'Joen, M. De Paepe, Probabilistic mapping of adiabatic horizontal two-phase flow by capacitance signal feature clustering, International Journal of Multiphase Flow 35 (7) (2009) 650-660.
17. H. Canière, Flow Pattern Mapping of Horizontal Evaporating Refrigerant Flow Based on Capacitive Void Fraction Measurements, PhD thesis, Ghent University - UGent, Gent, Belgium, 2009.
18. S.X. Yang, W.Q. Yang, A portable stray-immune capacitance meter, Review of Scientific Instruments 73 (4) (2002) 1958-1961.
19. L. Wojtan, T. Ursenbacher, J.R. Thome, Investigation of flow boiling in horizontal tubes: Part I - A new diabatic two-phase flow pattern map, International Journal of Heat and Mass Transfer 48 (14) (2005) 2955-2969.
20. P. Barbieri, J. Jabardo, E. Bandarra Filho, Flow patterns in convective boiling of refrigerant R-134a in smooth tubes of several diameters, Proceedings of the 5th European Thermal-Sciences Conference, Eindhoven, The Netherlands, 2008.
21. J. Drahos, J. Cermak, Diagnostics of Gas-Liquid Flow Patterns in Chemical-Engineering Systems, Chemical Engineering and Processing 26 (2) (1989) 147-164.
22. J. Shawe-Taylor, N. Cristianini, Kernel methods for pattern analysis, Cambridge University Press, Cambridge, UK, 2004.
23. I.T. Jolliffe, Principal Component Analysis, Springer, 2002.
24. J.C. Bezdek, Pattern Recognition with Fuzzy Objective Function Algorithms, Plenum Press, New York, USA, 1981, pp. 256.
25. L. Wojtan, T. Ursenbacher, J.R. Thome, Investigation of flow boiling in horizontal tubes: Part II - Development of a new heat transfer model for stratified-wavy, dryout and mist flow regimes, International Journal of Heat and Mass Transfer 48 (14) (2005) 2970-2985.

List of Figures

Figure 1

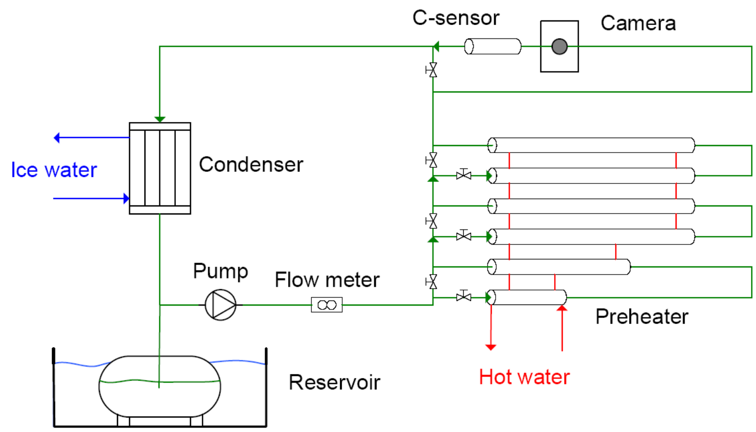
C-sensor
Camera
Ice water
Condenser
Pump
Flow meter
Preheater
Reservoir
Hot water

Figure 2

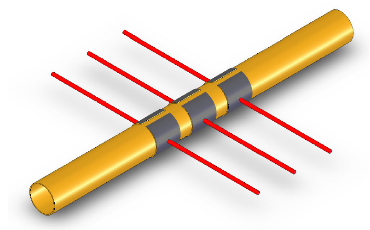

Figure 3

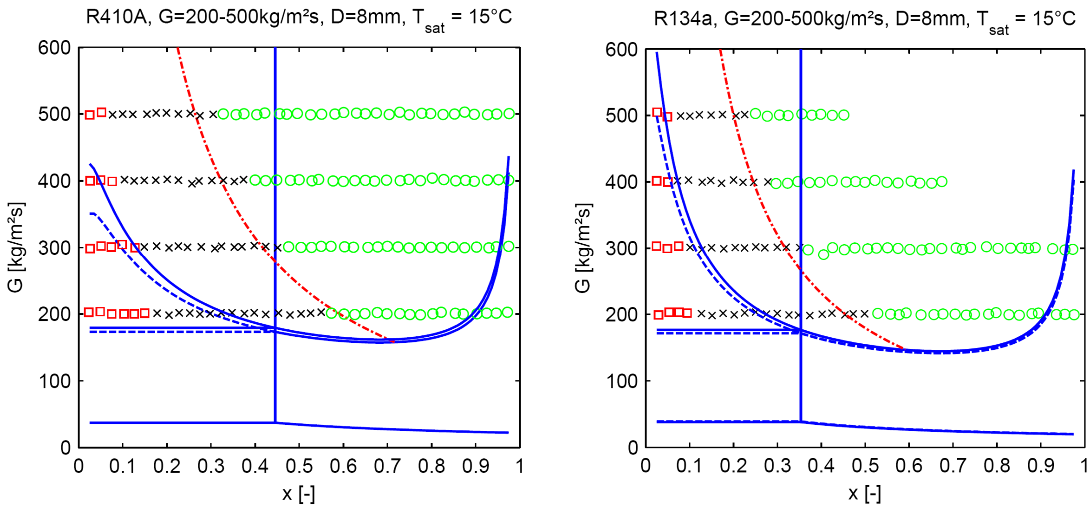

R410A, G=200-500kg/m²s, D=8mm, T_{sat} = 15°C
G [kg/m²s]
x [-]
R134a, G=200-500kg/m²s, D=8mm, T_{sat} = 15°C
G [kg/m²s]
x [-]

Figure 4

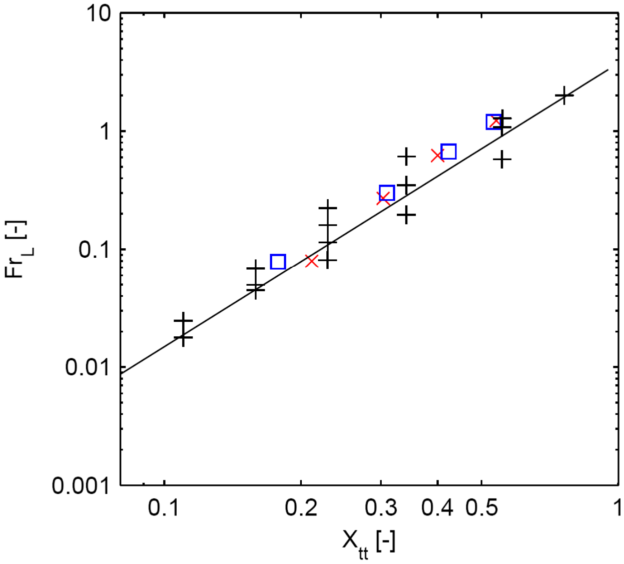

Figure 5

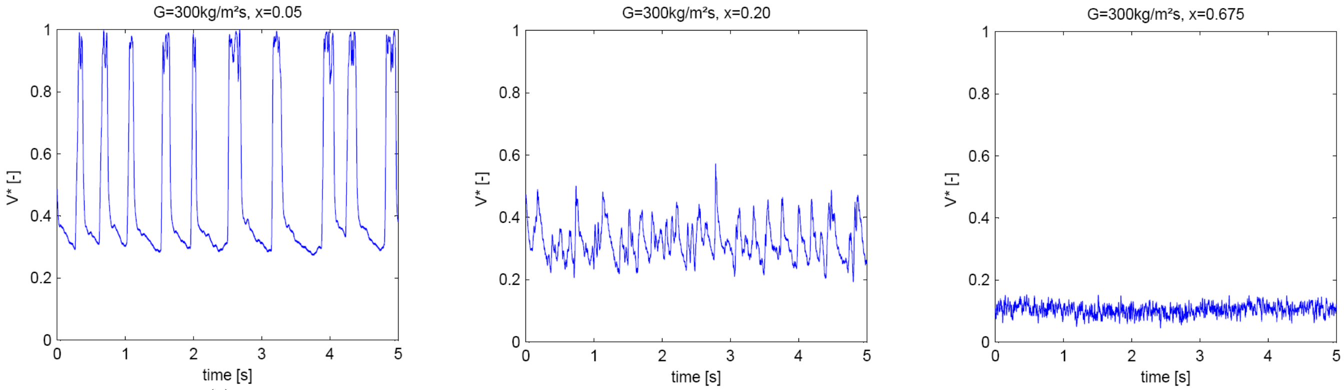
G=300kg/m²s, x=0.05
G=300kg/m²s, x=0.20
G=300kg/m²s, x=0.675
V* [-]
time [s]
0
0.2
0.4
0.6
0.8
1
0
1
2
3
4
5

(a) (b) (c)

Figure 6

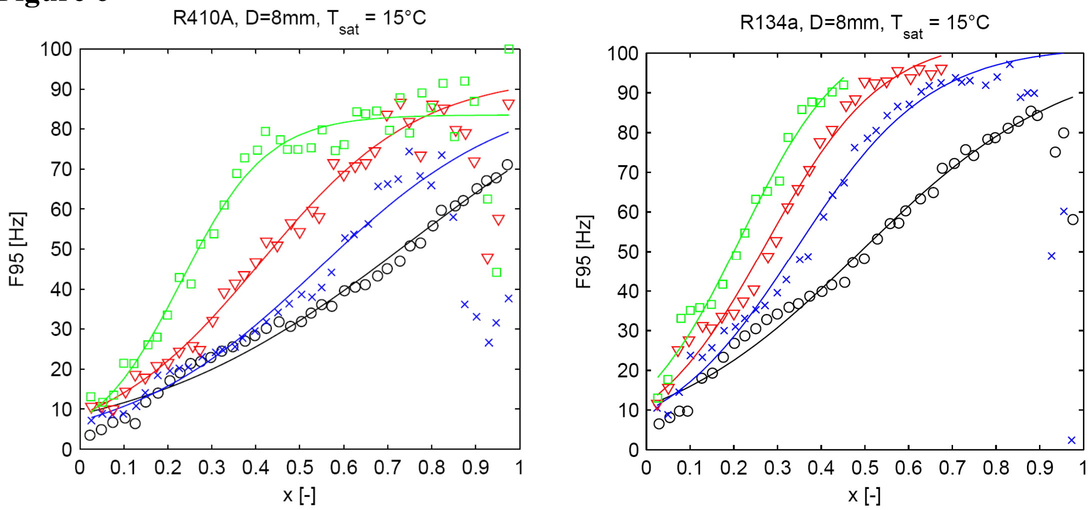

Figure 7

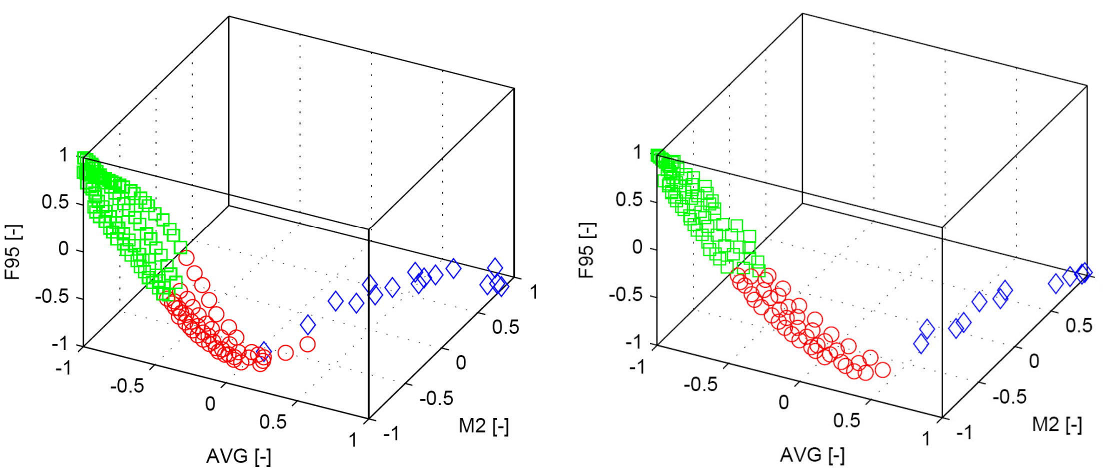

1
0.5
0
-0.5
-1
F95 [-]
-1
-0.5
0
0.5
1
AVG [-]
-1
-0.5
0
0.5
1
M2 [-]
1
0.5
0
-0.5
-1
F95 [-]
-1
-0.5
0
0.5
1
AVG [-]
-1
-0.5
0
0.5
1
M2 [-]

Figure 8

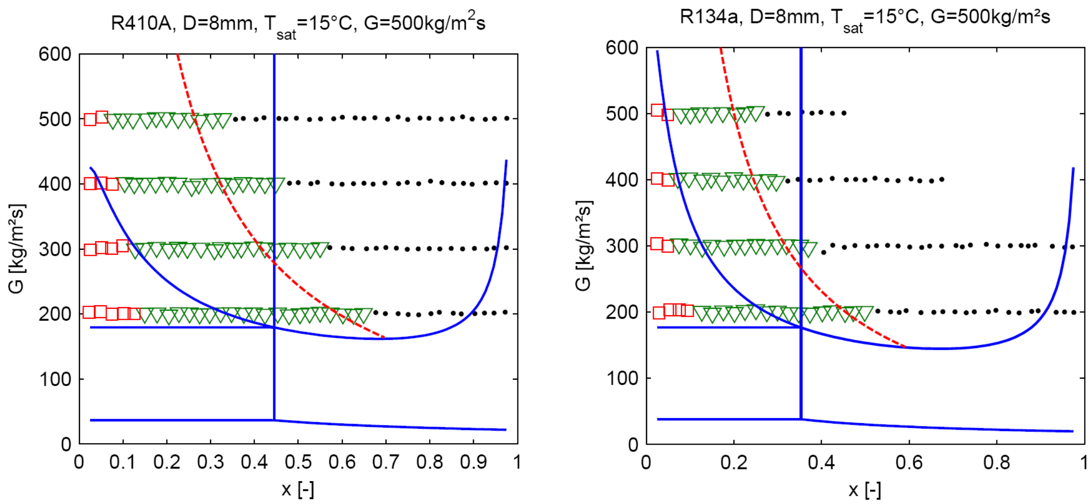
R410A, D=8mm, T_sat=15°C, G=500kg/m²s
G [kg/m²s]
x [-]
R134a, D=8mm, T_sat=15°C, G=500kg/m²s
G [kg/m²s]
x [-]

Figure 9

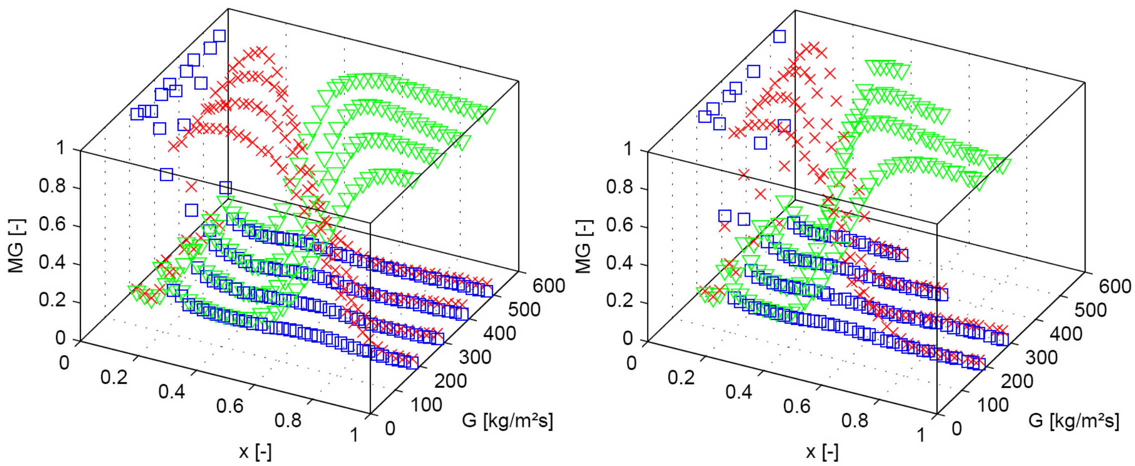

MG [-]
x [-]
G [kg/m²s]
1
0.8
0.6
0.4
0.2
0
0.2
0.4
0.6
0.8
1
600
500
400
300
200
100
0
MG [-]
x [-]
G [kg/m²s]

Figure 10

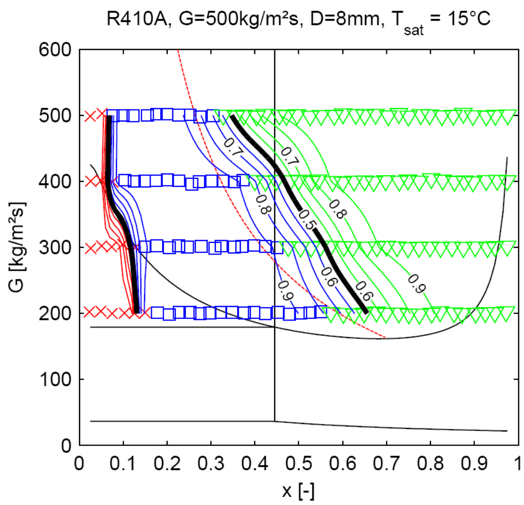

R410A, G=500kg/m²s, D=8mm, T_{sat} = 15°C
G [kg/m²s]
x [-]

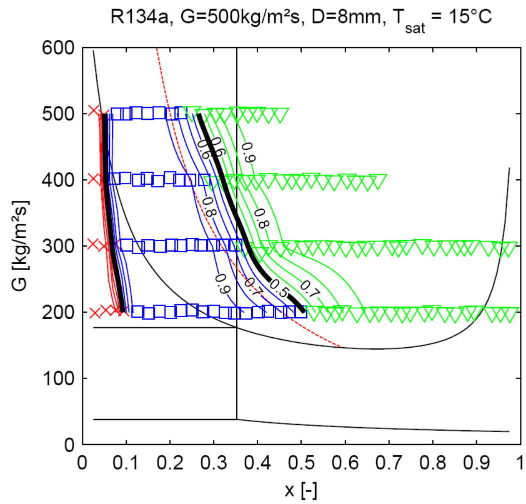

R134a, G=500kg/m²s, D=8mm, T_{sat} = 15°C
G [kg/m²s]
x [-]

Table 1: Results of the Fisher Criterion on the R410A signal features

Feature	All data	S/non-S	S-I only	A/non-A	I-A only
AVG	**3.676**	2.645	1.811	**1.804**	**2.553**
M2	**3.399**	**4.958**	**4.578**	0.200	0.385
M3	0.391	0.585	0.374	0.890	0.020
M4	0.017	0.014	0.002	0.021	0.018
F50	1.056	0.655	1.006	0.903	0.806
F70	1.303	0.666	1.034	1.275	1.180
F90	3.091	1.275	1.254	2.875	2.613
F95	**3.397**	1.540	1.210	**3.104**	**2.797**
F99	6.540	2.720	1.404	1.936	1.678

Table 2: Results of the Fisher Criterion on the R134a signal features

Feature	All data	S/non-S	S-I only	A/non-A	I-A only
AVG	**6.737**	3.599	2.886	**1.911**	2.440
M2	**3.378**	**3.738**	**3.499**	0.178	2.708
M3	1.384	1.950	2.419	0.032	0.012
M4	0.174	0.233	0.282	0.002	0.035
F50	2.124	0.842	1.041	2.277	2.138
F70	2.417	0.947	1.165	2.485	2.320
F90	4.065	1.340	1.324	3.580	3.360
F95	**5.575**	1.684	1.435	**3.810**	**3.651**
F99	3.067	1.715	0.633	1.460	1.214

Table 3: Coefficients of the first principle component of the feature data

Feature	R410A	R134a
AVG	-0.343	-0.260
M2	-0.234	-0.118
M3	-0.100	-0.058
M4	-0.035	-0.022
F50	0.235	0.349
F70	0.315	0.348
F90	0.434	0.356
F95	0.490	0.349
F99	0.483	0.294

Table 4: Variances and weight parameters by feature (after normalization)

Feature k	R410A var_k	R410A w_k	R134a var_k	R134a w_k
AVG	0.214	2.33	0.269	1.86
M2	0.216	2.31	0.168	2.98
F95	0.415	1.21	0.412	1.21

Table 5: Regression coefficients with R-squared values and scaling factors of R410A

G [kg/m²s]		200	300	400	500
S	a	-0.962	-0.982	-0.993	-0.997
	b	113.2	51.04	99.57	113.5
	c	1.87e6	269.7	425.4	1500
	P_0	0.968	0.984	0.996	1.005
	R^2	0.9994	0.9978	0.9986	0.9977
	p_{min}	5.67e-3	1.34e-3	3.37e-3	7.46e-3
	$1-p_{max}$	3.21e-2	1.63e-2	3.89e-3	-4.61e-3
A	a	13.97	18.30	20.85	19.91
	b	0.657	0.562	0.468	0.347
	R^2	0.999	0.9997	0.9996	0.9977
	p_{min}	1.04e-4	3.40e-5	5.77e-5	1.00e-3
	$1-p_{max}$	8.20e-3	3.30e-4	1.52e-5	2.24e-6
I	R^2	0.9979	0.9988	0.9991	0.9966

Table 6: Regression coefficients with R-squared values and scaling factors of R134a

G [kg/m²s]		200	300	400	500
S	a	-0.986	-0.983	-0.928	-0.987
	b	83.02	100.4	127.3	103.1
	c	1482	652.7	559.8	127.5
	P_0	0.992	0.987	0.933	0.990
	R^2	0.999	0.9998	0.9997	0.9997
	p_{min}	6.55e-3	4.03e-3	5.74e-3	3.08e-3
	$1-p_{max}$	7.88e-3	12.7e-3	6.66e-2	9.67e-3
A	a	15.84	27.18	30.03	28.77
	b	0.507	0.378	0.321	0.265
	R^2	0.994	0.9995	0.9997	0.996
	p_{min}	3.24e-4	3.45e-5	6.22e-5	4.87e-4
	$1-p_{max}$	4.09e-4	4.57e-8	1.39e-9	6.60e-10
I	R^2	0.994	0.9998	0.9992	0.996